

Chiral magnetic effect in ZrTe₅

Qiang Li^{1*}, Dmitri E. Kharzeev^{2,3*}, Cheng Zhang¹, Yuan Huang⁴, I. Pletikosić^{1,5}, A. V. Fedorov⁶, R. D. Zhong¹, J. A. Schneeloch¹, G. D. Gu¹ and T. Valla^{1*}

The chiral magnetic effect is the generation of an electric current induced by chirality imbalance in the presence of a magnetic field. It is a macroscopic manifestation of the quantum anomaly^{1,2} in relativistic field theory of chiral fermions (massless spin 1/2 particles with a definite projection of spin on momentum)—a remarkable phenomenon arising from a collective motion of particles and antiparticles in the Dirac sea. The recent discovery^{3–6} of Dirac semimetals with chiral quasiparticles opens a fascinating possibility to study this phenomenon in condensed matter experiments. Here we report on the measurement of magnetotransport in zirconium pentatelluride, ZrTe₅, that provides strong evidence for the chiral magnetic effect. Our angle-resolved photoemission spectroscopy experiments show that this material's electronic structure is consistent with a three-dimensional Dirac semimetal. We observe a large negative magnetoresistance when the magnetic field is parallel with the current. The measured quadratic field dependence of the magnetoconductance is a clear indication of the chiral magnetic effect. The observed phenomenon stems from the effective transmutation of a Dirac semimetal into a Weyl semimetal induced by parallel electric and magnetic fields that represent a topologically non-trivial gauge field background. We expect that the chiral magnetic effect may emerge in a wide class of materials that are near the transition between the trivial and topological insulators.

The recent discovery of the three-dimensional (3D) Dirac semimetals Cd₃As₂ and Na₃Bi (refs 3–6) has enabled experimental studies of the quantum dynamics of relativistic field theory in condensed matter systems. The relativistic theory of charged chiral fermions in three spatial dimensions possesses the so-called chiral anomaly^{1,2}—non-conservation of chiral charge induced by external gauge fields with non-trivial topology, for example, by parallel electric and magnetic fields. The existence of chiral quasiparticles in Dirac and Weyl semimetals opens the possibility to observe the effects of the chiral anomaly⁷. Of particular interest is the chiral magnetic effect (CME; ref. 8)—the generation of electric current in an external magnetic field induced by the chirality imbalance⁹.

This phenomenon is at present under intense study in relativistic heavy ion collisions at the Relativistic Heavy Ion Collider (RHIC) at BNL and at the Large Hadron Collider (LHC) at CERN, where it was predicted¹⁰ to induce fluctuations in hadron charge asymmetry with respect to the reaction plane. The experimental data from the STAR (ref. 11) Collaboration at RHIC and the ALICE (ref. 12) Collaboration at LHC indicate the fluctuations are consistent with the theoretical expectations. Closely related phenomena are expected to play an important role in the Early Universe, possibly

causing the generation of primordial magnetic fields^{13–17}. However, the interpretation in all these cases is under debate owing to lack of control over the chirality imbalance produced.

The most prominent signature of the CME in Dirac systems in parallel electric and magnetic fields is a positive contribution to the conductivity that has a quadratic dependence on magnetic field^{8,18,19}. This is because the CME current is proportional to the product of the chirality imbalance and the magnetic field, and the chirality imbalance in Dirac systems is generated dynamically through the anomaly with a rate that is proportional to the product of electric and magnetic fields. As a result, the longitudinal magnetoresistance becomes negative^{18,19}.

Let us explain how this mechanism works in Dirac semimetals in more detail. In the absence of external fields, each Dirac point initially contains left- and right-handed fermions with equal chemical potentials, $\mu_L = \mu_R = 0$. If the energy degeneracy between the left- and right-handed fermions gets broken, we can parameterize it by introducing the chiral chemical potential $\mu_5 \equiv (\mu_R - \mu_L)/2$. The corresponding density of chiral charge is then given by⁸

$$\rho_5 = \frac{\mu_5^3}{3\pi^2 v^3} + \frac{\mu_5}{3v^3} \left(T^2 + \frac{\mu^2}{\pi^2} \right) \quad (1)$$

where $\mu = (\mu_R + \mu_L)/2$ and T are the chemical potential and the temperature, and v is the Fermi velocity.

The chiral anomaly of quantum electrodynamics dictates that the parallel external electric and magnetic fields generate the chiral charge with a rate given by

$$\frac{d\rho_5}{dt} = \frac{e^2}{4\pi^2 \hbar^2 c} \mathbf{E} \cdot \mathbf{B} \quad (2)$$

However, the left- and right-handed fermions in Dirac semimetals can mix through chirality-changing scattering, and this process will deplete the amount of chiral charge that can be produced. Denoting the chirality-changing scattering time by τ_v , we thus get the equation

$$\frac{d\rho_5}{dt} = \frac{e^2}{4\pi^2 \hbar^2 c} \mathbf{E} \cdot \mathbf{B} - \frac{\rho_5}{\tau_v} \quad (3)$$

The solution of equation (3) at $t \gg \tau_v$ is

$$\rho_5 = \frac{e^2}{4\pi^2 \hbar^2 c} \mathbf{E} \cdot \mathbf{B} \tau_v \quad (4)$$

¹Condensed Matter Physics and Materials Science Department, Brookhaven National Lab, Upton, New York 11973, USA. ²Department of Physics, Brookhaven National Laboratory, Upton, New York 11973, USA. ³Department of Physics and Astronomy, Stony Brook University, New York 11794-3800, USA. ⁴Center for Functional Nanomaterials, Brookhaven National Lab, Upton, New York 11973, USA. ⁵Department of Physics, Princeton University, Princeton, New Jersey 08544, USA. ⁶Advanced Light Source, Lawrence Berkeley National Laboratory, Berkeley, California 94720, USA.

*e-mail: qiangli@bnl.gov; dmitri.kharzeev@stonybrook.edu; valla@bnl.gov

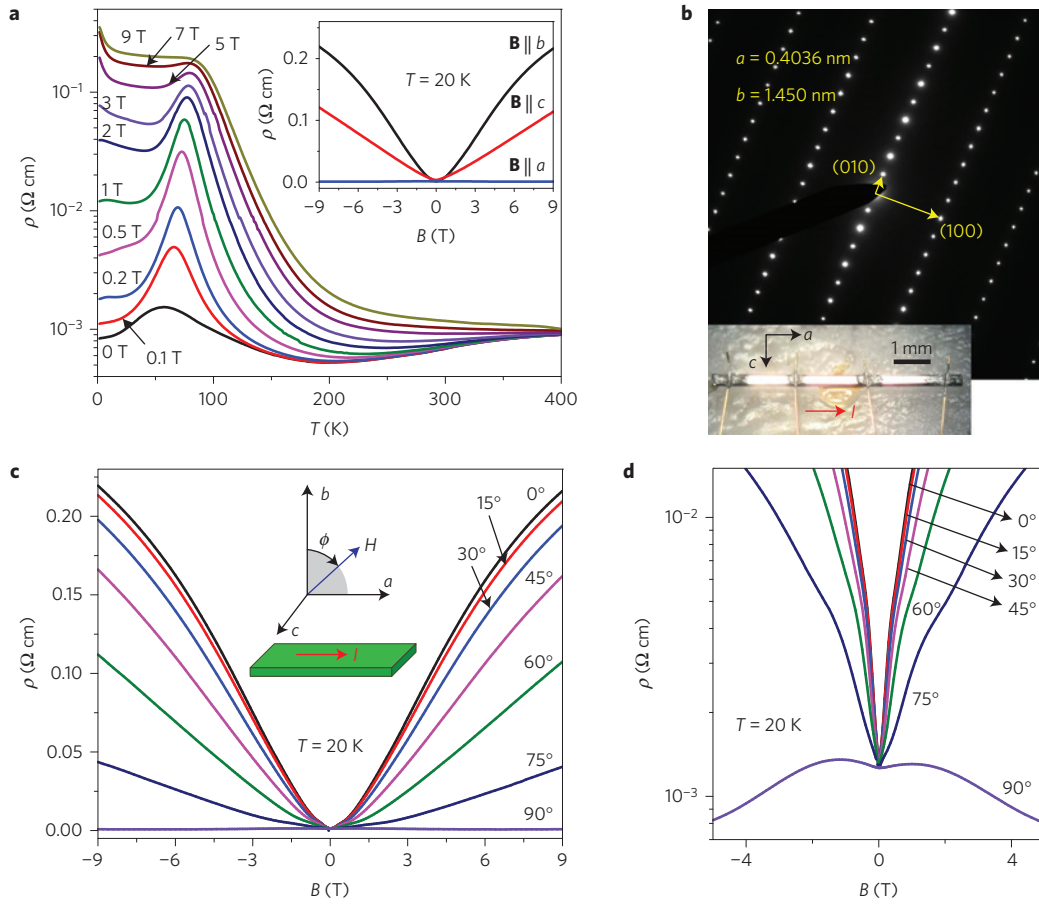


Figure 1 | Magnetoresistance in ZrTe₅. **a**, Temperature dependence of resistivity in ZrTe₅ in magnetic fields perpendicular to the cleavage plane (**B** || **b**). The inset shows the resistivity with the magnetic field applied along the three major crystal axes. **b**, Electron diffraction from a single crystal looking down the (001) direction. The inset shows the single crystal with the contacts for transport measurements. **c**, Magnetoresistance at 20 K for several angles of the applied field with respect to the current, as depicted in the inset. **d**, Same data as in **c**, plotted on a logarithmic scale, emphasizing the contrast between the extremely large positive magnetoresistance for the magnetic field perpendicular to the current (**B** || **b**) and the negative magnetoresistance for the magnetic field parallel to the current (**B** || **a**).

According to equation (1), this leads to a non-zero chiral chemical potential μ_5 (we assume that $\mu_5 \ll \mu, T$):

$$\mu_5 = \frac{3 v^3}{4 \pi^2} \frac{e^2}{\hbar^2 c} \frac{\mathbf{E} \cdot \mathbf{B}}{T^2 + \frac{\mu^2}{\pi^2}} \tau_V \quad (5)$$

On the lowest Landau level, the spins of positive (negative) chiral fermions are parallel (anti-parallel) to the external magnetic field. Therefore, for a positive fermion to be right-handed (that is, have a positive projection of spin on momentum) it means moving along the magnetic field, whereas for a negative fermion it means moving against the magnetic field. The left-handed fermions will move in the opposite directions, so there will normally be no charge separation. However, if the densities of the right- and left-handed fermions are different, the currents of positive and negative charges do not compensate each other, and the system develops a net electric current—this is the CME. The corresponding current can be computed⁸ by field-theoretical methods and is given by

$$\mathbf{J}_{\text{CME}} = \frac{e^2}{2\pi^2} \mu_5 \mathbf{B} \quad (6)$$

The formulae (6) and (5) yield the final expression for the CME current:

$$J_{\text{CME}}^i = \frac{e^2}{\pi \hbar} \frac{3}{8} \frac{e^2}{\hbar c} \frac{v^3}{\pi^3} \frac{\tau_V}{T^2 + \frac{\mu^2}{\pi^2}} B^j B^k E^k \equiv \sigma_{\text{CME}}^{ik} E^k \quad (7)$$

We see that the CME is described by the conductivity tensor $\sigma_{\text{CME}}^{ik} \sim B^j B^k$. When the electric and magnetic fields are parallel, the CME conductivity is

$$\sigma_{\text{CME}}^{zz} = \frac{e^2}{\pi \hbar} \frac{3}{8} \frac{e^2}{\hbar c} \frac{v^3}{\pi^3} \frac{\tau_V}{T^2 + \frac{\mu^2}{\pi^2}} B^2 \quad (8)$$

Because the CME current is directed along the electric field, it will affect the measured conductivity, as the total current will be the sum of the Ohmic and CME currents:

$$\mathbf{J} = \mathbf{J}_{\text{Ohm}} + \mathbf{J}_{\text{CME}} = (\sigma_{\text{Ohm}} + \sigma_{\text{CME}}) \mathbf{E} \quad (9)$$

where $\sigma_{\text{CME}} \equiv \sigma_{\text{CME}}^{zz}$. If the electric and magnetic fields are parallel ($\theta = 0$), there is no conventional contribution to magnetoresistance induced by the Lorentz force. The magnetoconductance (8) has a characteristic quadratic dependence on magnetic field. It is precisely this contribution to magnetoconductance with a quadratic dependence on magnetic field that we have unambiguously observed in ZrTe₅.

ZrTe₅ is a material that crystallizes in the layered orthorhombic crystal structure, with prismatic ZrTe₆ chains running along the crystallographic *a*-axis and linked along the *c*-axis by zigzag chains of Te atoms to form two-dimensional (2D) layers, stacked along the *b*-axis into a crystal. This material is known for its large thermoelectric power, resistivity anomaly²⁰ and large positive

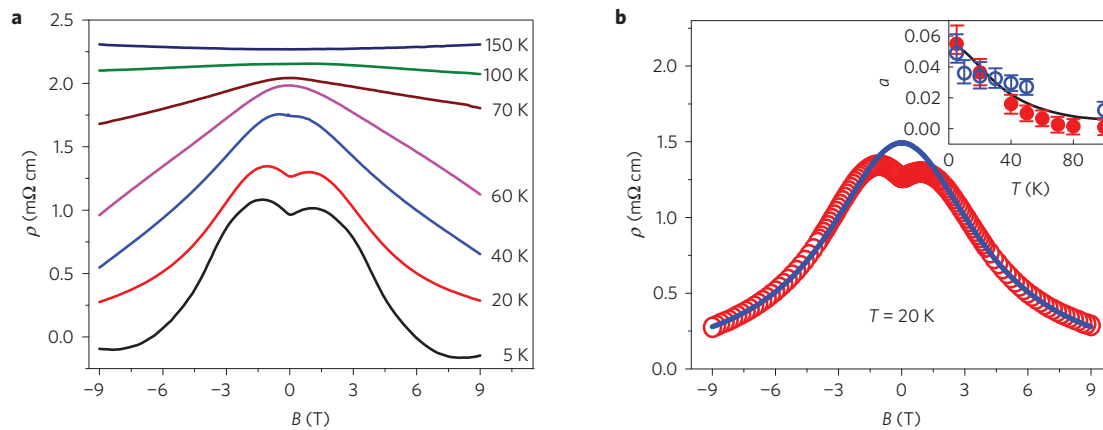


Figure 2 | Magnetoresistance in magnetic fields parallel to the current ($B \parallel a$) in $ZrTe_5$. **a**, Magnetoresistance at various temperatures. For clarity, the resistivity curves have been shifted by $1.5 \text{ m}\Omega \text{ cm}$ (150 K), $0.9 \text{ m}\Omega \text{ cm}$ (100 K), $0.2 \text{ m}\Omega \text{ cm}$ (70 K) and $-0.2 \text{ m}\Omega \text{ cm}$ (5 K). **b**, Magnetoresistance at 20 K (red symbols) fitted with the CME curve (blue line); inset: temperature dependence of the parameter $a(T)$ in units of $\text{S cm}^{-1} \text{T}^{-2}$ for B and E along the a -axis (red solid symbols), and 18° off the a -axis within the a - c plane (open circles). The line represents the dependence predicted by equation (8).

magnetoresistance²¹. It shows a semimetallic electronic structure with extremely small and light ellipsoidal Fermi surface(s), centred at the centre (Γ point) of the bulk Brillouin zone (BZ). The calculations predict a small direct gap at Γ ($\cong 50 \text{ meV}$), but previous transport studies show semimetallic behaviour, with quantum oscillations indicating a tiny but finite Fermi surface^{22–25}. Quantum oscillations show that the effective mass in the chain direction ($m_a^*/m_e \cong 0.03$) is comparable to that in a prototypical 3D Dirac semimetal, Cd_3As_2 (refs 24,26).

Figure 1a shows the temperature dependence of resistivity along the chain direction (a) in a magnetic field perpendicular to the a - c plane. The zero-field transport shows a characteristic peak in resistivity at $T \cong 60 \text{ K}$, significantly lower than in earlier studies, probably due to a much lower impurity concentration in our samples²⁰. In $B \parallel b$, the peak shifts to higher temperatures and we observe a very large positive magnetoresistance in the whole temperature range, consistent with previous studies²¹. The inset shows the resistivity with the magnetic field applied along the three major crystal axes.

Figure 1c,d shows the magnetoresistance measured at 20 K for several angles of the applied magnetic field with respect to the current along the chain direction. The angle rotates from the b -axis to the a -axis, so that at $\varphi = 90^\circ$ the field is parallel to the current ($B \parallel a$)—the so-called Lorentz-force-free configuration. When the magnetic field is aligned along the b -axis ($\varphi = 0^\circ$), the magnetoresistance is positive and quadratic in low fields, and tends to saturate in high fields. The similar angular dependence is also observed for the field in the c - a plane. When the magnetic field is rotated away from the b - or c -axis, the positive magnetoresistance drops with $\cos \phi$, as expected for the Lorentz force component. However, in the Lorentz-force-free configuration ($B \parallel a$), we see a large negative magnetoresistance, a clear indication of CME in this material.

Figure 2 shows the magnetoresistance at various temperatures in a magnetic field parallel to the current. At elevated temperatures, $T \geq 110 \text{ K}$, the ρ versus B curves show a small upward curvature, a contribution from an inevitable perpendicular field component due to imperfect alignment between the current and the magnetic field. In fact, the small perpendicular field contribution to the observed resistivity can be fitted with a simple quadratic term (Supplementary Information and Supplementary Fig. 1). This term is treated as a background and subtracted from the parallel field component for all magnetoresistance curves recorded at $T \leq 100 \text{ K}$.

A negative magnetoresistance is observed for $T \leq 100 \text{ K}$, increasing in magnitude as temperature decreases. We found that the magnetic field dependence of the negative magnetoresistance can be nicely fitted with the CME contribution to the electrical

conductivity, given by $\sigma_{\text{CME}} = \sigma_0 + a(T)B^2$, where σ_0 represents the zero-field conductivity. The fitting is illustrated in Fig. 2b for $T = 20 \text{ K}$, with an excellent agreement between the data and the CME fitting curve. At 4 T, the CME conductivity is about the same as the zero-field conductivity. At 9 T, the total magnetoconductivity increases by $\sim 400\%$ over the zero-field value as a result of the CME contribution. This results in a negative magnetoresistance that is much stronger than any conventional magnetoresistance reported at an equivalent magnetic field in a non-magnetic material. To demonstrate that the effect is not limited to any specific crystal direction, but locked only to the current direction, we have also performed magnetoresistance measurements with the current still in the a - c plane, but 18° off the chain direction (a -axis). In this direction, we observe the same $\propto B^2$ dependence of CME when the magnetic field is parallel to the current.

To obtain a numerical theoretical estimate for CME, we take $T = 20 \text{ K}$, $\rho_{\text{ohm}} \cong 1.2 \text{ m}\Omega \text{ cm}$ indicated by our measurements at $B = 0$, and assume that the rate of chirality-changing transitions $\tau_v^{-1} = \Delta/\hbar$. $\Delta \cong 50 \text{ meV}$ and $\mu \cong 9 \text{ meV}$ is determined from the fit to the data. The ARPES data indicate that $v \cong 1/300 c$. Evaluating equation (8), we reproduce the correct order of magnitude of the coefficient $a(T)$ that we used to fit the quadratic dependence of magnetoresistance on magnetic field. The inset in Fig. 2b shows the temperature dependence of parameter $a(T)$ for B and E along the a -axis (red solid symbols) and 18° off the a -axis, in the a - c plane (open circles), together with the dependence (line) predicted by equation (8) in which the effective value of μ is found to be $\mu \sim 9 \text{ meV}$.

At very low field, the data show a small cusp-like feature. The origin of this feature is not completely understood, but it probably indicates some form of weak anti-localization (WAL). This, and the large positive magnetoresistance for magnetic field perpendicular to current, seem to be common features in all the materials that were subsequently found to exhibit the CME in parallel fields^{27–32}. Although the reason for a simultaneous observation of CME in parallel fields and large magnetoresistance in perpendicular fields is not fully understood yet, we note that the general requirements for the observation of CME—that is, the low carrier concentration and nearly linear bands—seem to be also favourable for the observation of large positive magnetoresistance in perpendicular fields. In these situations, the system is either very close to the quantum limit³³ or, if it contains two types of carriers, the charge compensation may lead to a large response in the way that was recently observed in WTe_2 (refs 34–36).

A necessary requirement for observation of the CME is that a material has a 3D Dirac semimetal-like (zero gap), or semiconductor-like (non-zero gap) electronic structure. Figure 3

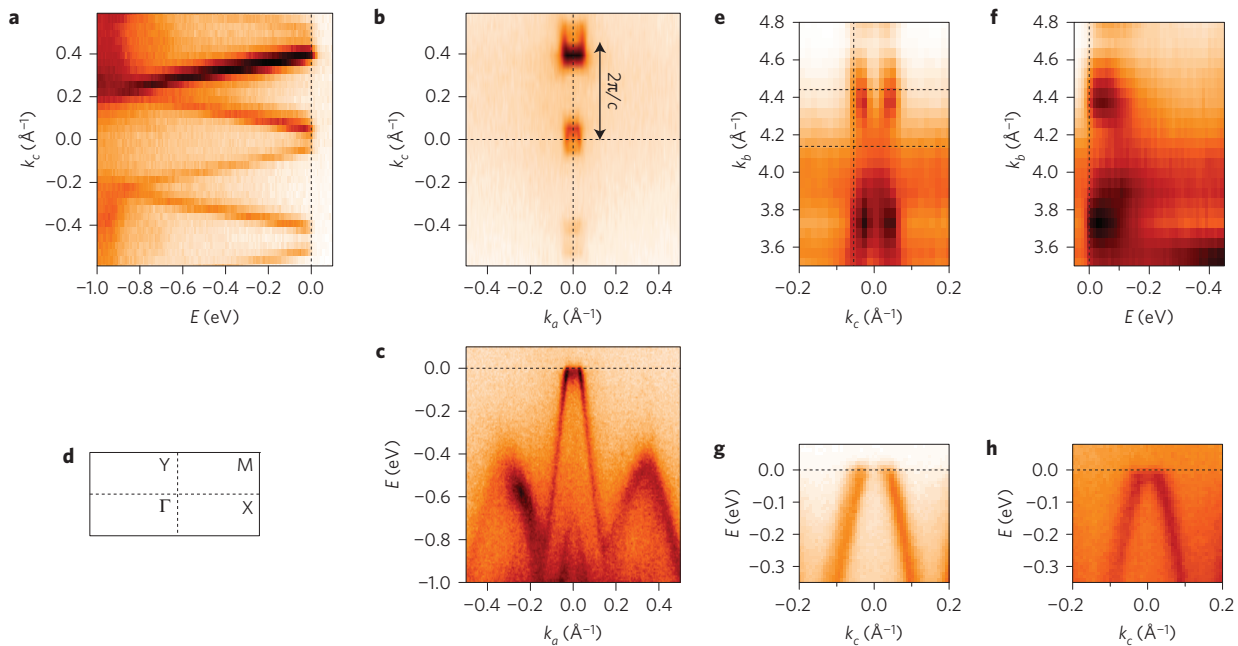


Figure 3 | Electronic structure of ZrTe₅. **a–c**, In-plane. **a**, Valence band dispersion along the $\bar{\Gamma}$ – \bar{Y} momentum line (perpendicular to the chain direction). The second BZ $\bar{\Gamma}$ points are visible at $k_c = \pm 0.454 \text{ \AA}^{-1}$. **b**, Constant energy contour of the ARPES intensity at $E = 0$ (FS) as a function of the in-plane momentum. **c**, Valence band dispersion along the $\bar{\Gamma}$ – \bar{X} (chain direction). Spectra in panels **a–c** were recorded at $h\nu = 63 \text{ eV}$ photon energy and $T = 20 \text{ K}$. **d**, Schematic view of the surface BZ. **e–h**, Out-of-plane. **e**, Fermi surface contour as a function of the in-plane momentum perpendicular to the chain, k_c , and the momentum perpendicular to the surface, k_b . **f**, Dispersion perpendicular to the surface at $k_0 = 0$, $k_c = -0.055 \text{ \AA}^{-1}$ (vertical dashed line in **e**). The horizontal dashed lines correspond to the two perpendicular momenta where the in-plane electronic structure is probed in **g** and **h**. **g, h**, Dispersion perpendicular to the chain direction at $k_0 = 0$, $k_b = 4.43 \text{ \AA}^{-1}$ (**g**) and at $k_0 = 0$, $k_c = 4.13 \text{ \AA}^{-1}$ (**h**).

shows angle-resolved photoemission spectroscopy (ARPES) data from a freshly cleaved (a – c plane) ZrTe₅ sample. The states forming the small, hole-like Fermi surface (FS) disperse linearly over a large energy range, both along the chain direction (Fig. 3c) and perpendicular to it (Fig. 3a), indicating a Dirac-like dynamics of carriers for the in-plane propagation. The velocity, or the slope of dispersion, is very large in both the chain direction, $v_a \cong 6.4 \text{ eV \AA}$ ($\cong c/300$), and perpendicular to it, $v_c \cong 4.5 \text{ eV \AA}$. If extrapolated to the unoccupied part, the linear approximation for this band would place the Dirac point at $\sim 0.2 \text{ eV}$ above the E_F .

In Fig. 3c, it also seems that the bottom of a tiny electron pocket is enclosed by the dominant hole-cone. However, owing to a sizable quasiparticle scattering, $\Gamma_Q = \hbar/\tau_Q \cong 100 \text{ meV}$, the states are apparently too broad to completely resolve possible fine features in the low-energy electronic structure, such as the existence of small gaps or changes in the velocity at low energies ($E < 50 \text{ meV}$). Nevertheless, the magnitude of CME in ZrTe₅ is not particularly sensitive to the fine details in the electronic structure on an energy scale smaller than Γ_Q . On the other hand, for the existence of CME, it is crucial that the electronic structure of a material is 3D Dirac-like. Although recent magneto-optical studies have shown that ZrTe₅ is indeed a 3D Dirac semimetal³⁷, it has been also suggested that this material might be either a weak or strong topological insulator²⁵. It is therefore important to verify that the states seen in ARPES are bulk states and not topological surface states.

This is done in Fig. 3e–h, which shows the dependence of the states forming the FS on the momentum k_b perpendicular to the a – c plane. Figure 3e, f shows a clear warping of the Fermi surface and a significant dispersion with k_b , indicating the bulk character of the measured states. Unfortunately, because the Dirac point is unoccupied, the ARPES studies cannot provide a complete picture of the electronic structure in its vicinity, and the existence of a small mass gap cannot be excluded. The occupied part of the cone (Fig. 3f–h) indicates that the out-of-plane velocity is an order of

magnitude smaller than the in-plane velocity, consistent with ZrTe₅ being a highly anisotropic 3D Dirac semimetal.

We note that the possible coexistence of both the hole and electron pockets might be responsible for the large positive magnetoresistance seen in the perpendicular field, as the fine balance between them could lead to a perfect compensation at some temperature^{34–36}. We also note that the tiny volume of the FS indicates a very low carrier concentration, 10^{17} – 10^{18} cm^{-3} , consistent with the absence of quantum oscillations in transport measurements in the probed field range.

As noted, the ARPES measurements cannot exclude a possible gap in the otherwise Dirac-like spectrum. The gap Δ will in general induce chirality-changing transitions with a rate Δ/\hbar —this is because the corresponding term in the effective Hamiltonian, namely $\Delta(\bar{\Psi}_L \bar{\Psi}_R + \bar{\Psi}_R \bar{\Psi}_L)$, mixes the left and right components of the spinors—but it does not prevent the CME. The ARPES data also indicate that the quantum scattering rate determined from the broadening of quasiparticles is $\Gamma_Q = \hbar/\tau_Q \cong 100 \text{ meV}$. Chirality conservation in the quasiparticle scattering processes implies that the chirality-changing rate should be only a small fraction of the quantum scattering rate, $\Gamma_V = \hbar/\tau_V \ll \Gamma_Q$. It is therefore reasonable to assume that the measured Γ_Q represents the absolute upper limit to the chirality-changing transition rate. The existence of intra-valley transitions does not destroy the CME, although the chirality-flipping transitions do reduce the magnitude of the CME current, as can be seen in our equation (8) for the CME conductivity, which is inversely proportional to the chirality-flipping rate.

We note that equation (9) shows that, in the regime where $\rho_{\text{ohm}} \gg \rho_{\text{CME}}$, the measured magnetoresistivity ρ directly provides the CME resistivity, $\rho \cong \rho_{\text{CME}}$. Therefore it is much easier to observe the CME in materials that have a relatively large zero-field resistivity. The zero-field resistivity in ZrTe₅ is $\rho_{\text{ohm}} \cong 1.2 \text{ m}\Omega \text{ cm}$ at $T = 20 \text{ K}$, and according to our theoretical estimates the CME and Ohmic resistivities become equal, $\rho_{\text{ohm}} \cong \rho_{\text{CME}}$, at $B \cong 3 \text{ T}$. On the

other hand, if a material had a much smaller resistivity, the CME observation would have been more difficult.

The present study can be extended to a broad range of materials as 3D Dirac semimetals often emerge at quantum transitions between conventional ('trivial') and topological insulators, and between conventional and topological crystalline insulators. Indications that the CME occurs at the former type of transitions have already been observed in $\text{Bi}_{1-x}\text{Sb}_x$ at $x \approx 0.03$ (ref. 33). In addition, our experimental observation has important implications extending well beyond condensed matter physics.

Note added in proof: After submission of our manuscript, we noticed a surging interest in the study of magnetotransport in Dirac-like semimetals, with several recent preprints reporting a negative magnetoresistance as a consequence of the CME. The effect is observed in two types of 3D chiral materials. The first type consists of Dirac semimetals, where the Dirac points for left- and right-handed fermions are not separated in momentum space. These materials are effectively transformed into Weyl semimetals by parallel electric and magnetic fields, with an imbalance between the densities of left- and right-handed fermions induced by the chiral anomaly. Members of that class are ZrTe_5 , Na_3Bi (ref. 27), Cd_3As_2 (ref. 32) and $\text{Bi}_{1-x}\text{Sb}_x$ ($x \approx 0.03$; ref. 33). In particular, a very detailed transport measurement was performed recently with the Dirac semimetal Na_3Bi (ref. 27), with results similar to ours. They observed both a cusp of longitudinal magnetoresistance near zero magnetic field and a negative longitudinal magnetoresistance in stronger fields due to the CME, with a steep dependence on the angle between electric and magnetic fields²⁷. The second type of 3D chiral materials consists of inversion asymmetric Weyl semimetals, such as TaAs (ref. 28), NbAs (ref. 29), NbP (ref. 30) and TaP (ref. 31). In both types of materials, parallel electric and magnetic fields are required to observe the CME.

Methods

Methods and any associated references are available in the [online version of the paper](#).

Received 19 December 2014; accepted 4 January 2016;
published online 8 February 2016

References

- Adler, S. L. Axial-vector vertex in spinor electrodynamics. *Phys. Rev.* **177**, 2426–2438 (1969).
- Bell, J. S. & Jackiw, R. A PCAC puzzle: $\pi^0 \rightarrow \gamma\gamma$ in the σ -model. *Il Nuovo Cimento A* **60**, 47–61 (1969).
- Wang, Z. *et al.* Dirac semimetal and topological phase transitions in A_3Bi ($\text{A} = \text{Na}, \text{K}, \text{Rb}$). *Phys. Rev. B* **85**, 195320 (2012).
- Wang, Z., Weng, H., Wu, Q., Dai, X. & Fang, Z. Three-dimensional Dirac semimetal and quantum transport in Cd_3As_2 . *Phys. Rev. B* **88**, 125427 (2013).
- Borisenko, S. *et al.* Experimental realization of a three-dimensional Dirac semimetal. *Phys. Rev. Lett.* **113**, 027603 (2014).
- Liu, Z. K. *et al.* Discovery of a three-dimensional topological Dirac semimetal, Na_3Bi . *Science* **343**, 864–867 (2014).
- Nielsen, H. B. & Ninomiya, M. The Adler–Bell–Jackiw anomaly and Weyl fermions in a crystal. *Phys. Lett. B* **130**, 389–396 (1983).
- Fukushima, K., Khazeev, D. & Warringa, H. Chiral magnetic effect. *Phys. Rev. D* **78**, 074033 (2008).
- Khazeev, D. E. The chiral magnetic effect and anomaly-induced transport. *Prog. Part. Nucl. Phys.* **75**, 133–151 (2014).
- Khazeev, D. Parity violation in hot QCD: Why it can happen, and how to look for it. *Phys. Lett. B* **633**, 260–264 (2006).
- Abelev, B. *et al.* Azimuthal charged-particle correlations and possible local strong parity violation. *Phys. Rev. Lett.* **103**, 251601 (2009).
- Abelev, B. *et al.* Charge separation relative to the reaction plane in Pb–Pb collisions at $\sqrt{s_{NN}} = 2.76$ TeV. *Phys. Rev. Lett.* **110**, 012301 (2013).
- Vilenkin, A. & Leahy, D. Parity nonconservation and the origin of cosmic magnetic fields. *Astrophys. J.* **254**, 77–81 (1982).
- Fröhlich, J. & Pedrini, B. New applications of the chiral anomaly. Preprint at <http://arxiv.org/abs/hep-th/0002195> (2000).

- Joyce, M. & Shaposhnikov, M. Primordial magnetic fields, right electrons, and the Abelian anomaly. *Phys. Rev. Lett.* **79**, 1193–1196 (1997).
- Giovannini, M. & Shaposhnikov, M. E. Primordial hypermagnetic fields and the triangle anomaly. *Phys. Rev. D* **57**, 2186–2206 (1998).
- Vachaspati, T. Estimate of the primordial magnetic field helicity. *Phys. Rev. Lett.* **87**, 251302 (2001).
- Son, D. T. & Spivak, B. Z. Chiral anomaly and classical negative magnetoresistance of Weyl metals. *Phys. Rev. B* **88**, 104412 (2013).
- Burkov, A. A. Chiral anomaly and diffusive magnetotransport in Weyl metals. *Phys. Rev. Lett.* **113**, 247203 (2014).
- Okada, S., Sambongi, T. & Ido, M. Giant resistivity anomaly in ZrTe_5 . *J. Phys. Soc. Jpn* **49**, 839–840 (1980).
- Tritt, T. *et al.* Large enhancement of the resistive anomaly in the pentatelluride materials HfTe_5 and ZrTe_5 with applied magnetic field. *Phys. Rev. B* **60**, 7816–7819 (1999).
- Whangbo, M., DiSalvo, F. & Fleming, R. Electronic structure of ZrTe_5 . *Phys. Rev. B* **26**, 687–689 (1982).
- McIlroy, D. N. *et al.* Observation of a semimetal–semiconductor phase transition in the intermetallic ZrTe_5 . *J. Phys. Condens. Matter* **16**, L359–L365 (2004).
- Kamm, G., Gillespie, D., Ehrlich, A., Wieting, T. & Levy, F. Fermi surface, effective masses, and Dingle temperatures of ZrTe_5 as derived from the Shubnikov–de Haas effect. *Phys. Rev. B* **31**, 7617–7623 (1985).
- Weng, H., Dai, X. & Fang, Z. Transition-metal pentatelluride ZrTe_5 and HfTe_5 . *Phys. Rev. X* **4**, 011002 (2014).
- He, L. P. *et al.* Quantum transport evidence for the three-dimensional Dirac semimetal phase in Cd_3As_2 . *Phys. Rev. Lett.* **113**, 246402 (2014).
- Xiong, J. *et al.* Evidence for the chiral anomaly in the Dirac semimetal Na_3Bi . *Science* **350**, 413–416 (2015).
- Huang, X. *et al.* Observation of the chiral-anomaly-induced negative magnetoresistance in 3d Weyl semimetal TaAs. *Phys. Rev. X* **5**, 031023 (2015).
- Yang, X., Li, Y., Wang, Z., Zhen, Y. & Xu, Z.-A. Observation of negative magnetoresistance and nontrivial π Berry's phase in 3D Weyl semi-metal NbAs. Preprint at <http://arxiv.org/abs/1506.02283> (2015).
- Wang, Z. *et al.* Helicity protected ultrahigh mobility Weyl fermions in NbP. Preprint at <http://arxiv.org/abs/1506.00924> (2015).
- Shekhar, C. *et al.* Large and unsaturated negative magnetoresistance induced by the chiral anomaly in the Weyl semimetal TaP. Preprint at <http://arxiv.org/abs/1506.06577> (2015).
- Li, C.-Z. *et al.* Giant negative magnetoresistance induced by the chiral anomaly in individual Cd_3As_2 nanowires. *Nature Commun.* **6**, 10137 (2015).
- Kim, H.-J. *et al.* Dirac versus Weyl fermions in topological insulators: Adler–Bell–Jackiw anomaly in transport phenomena. *Phys. Rev. Lett.* **111**, 246603 (2013).
- Pippard, A. *Magnetoresistance in Metals. Cambridge Studies in Low Temperature Physics* (Cambridge Univ. Press, 1989).
- Ali, M. N. *et al.* Large, non-saturating magnetoresistance in WTe_2 . *Nature* **514**, 205–208 (2014).
- Pletikosić, I., Ali, M. N., Fedorov, A. V., Cava, R. J. & Valla, T. Electronic structure basis for the extraordinary magnetoresistance in WTe_2 . *Phys. Rev. Lett.* **113**, 216601 (2014).
- Chen, R. Y. *et al.* Magnetoinfrared spectroscopy of Landau levels and Zeeman splitting of three-dimensional massless Dirac fermions in ZrTe_5 . *Phys. Rev. Lett.* **115**, 176404 (2015).

Acknowledgements

We thank J. Misewich, P. Johnson, A. Abanov and G. Monteiro for discussions. This work was supported by the US Department of Energy, Office of Basic Energy Sciences, contracts No. DE-AC02-98CH10886, No. DE-FG-88ER40388, Office of Nuclear Physics, contract No. DE-FG-88ER41723 and ARO MURI Program, grant W911NF-12-1-0461. ALS is operated by the US DOE under Contract No. DE-AC02-05CH11231.

Author contributions

D.E.K. designed and, with Q.L. and T.V., directed the study, analysed results, and wrote the manuscript. Q.L. and C.Z. performed the transport measurements and analysed results. R.D.Z., J.A.S. and G.D.G. grew the crystals and performed X-ray diffraction experiments, Y.H. performed the SEM/TEM measurements and provided analysis. I.P., A.V.F. and T.V. performed the ARPES measurements and analysed results. All authors made contributions to writing the manuscript.

Additional information

Supplementary information is available in the [online version of the paper](#). Reprints and permissions information is available online at www.nature.com/reprints. Correspondence and requests for materials should be addressed to Q.L. or D.E.K. or T.V.

Competing financial interests

The authors declare no competing financial interests.

Methods

Crystal growth. Crystals of ZrTe_5 were grown by the flux growth method using Te as flux. High-purity elements (99.99999% Te and 99.99999% Zr) were loaded into a double-walled quartz ampoule and sealed under vacuum. The composition of the Zr–Te melt used for the ZrTe_5 growth was $\text{Zr}_{0.0025}\text{Te}_{0.9975}$. The materials were first melted at 900 °C in a box furnace and fully rocked for 72 h to achieve a homogeneous mixture. The melt was then slowly cooled and rapidly heated (for re-melting of small size crystals) between 445 and 505 °C for 21 days. The largest single crystals were $\sim 0.1 \times 0.3 \times 20 \text{ mm}^3$. Crystals were chemically and structurally characterized by powder X-ray diffraction, scanning electron microscopy with energy dispersive X-ray analysis, and transmission electron microscopy with electron diffraction.

Transport measurements. The magnetoresistance of ZrTe_5 samples was measured using the four-point probe in-line method in a Quantum Design Physical Property Measurement System (PPMS) equipped with 9 T superconducting magnet. Measurements have been performed with the current along the chain direction (a) and 18° off the chain direction, but still in the a – c plane. The off a -axis measurements were extremely difficult, owing to the needle-like aspect of our single crystals and their small size along the c and b -axes. For crystal alignment with the magnetic field, horizontal and vertical sample rotators were used with an angular resolution of $\sim 0.1^\circ$. Temperature-dependent data were taken from 1.8 to 400 K, at various fields up to 9 T.

ARPES experiments. The ARPES measurements were conducted using a Scienta SES2002 analyser at the U13 beam line of the National Synchrotron Light Source at

Brookhaven National Laboratory ($h\nu = 21 \text{ eV}$), and at the 12.0.1 beam line of the Advanced Light Source at Lawrence Berkeley National Laboratory (35–80 eV) using a Scienta R 3000 analyzer. The total experimental resolution was $\cong 15 \text{ meV}$ in energy and $\leq 0.2^\circ$ in angle, in both experimental set-ups. The two-dimensional Brillouin zone mapping was accomplished by rotating the sample perpendicularly to the analyser slit, in steps of 1° at $h\nu = 21 \text{ eV}$ and 0.5° at higher photon energies. The samples were glued to the holder using a conductive epoxy resin and cleaved at the a – c plane in an ultrahigh vacuum ($p < 10^{-8} \text{ Pa}$) just before the measurements. Sample cooling was provided through contact with cryostats filled with liquid helium or liquid nitrogen.

The evolution of electronic structure with photon energy reflects the dispersion along k_z (k_b in our notation). Even though k_z is not conserved in a photoemission process, it can be approximated by $k_z = (1/\hbar)\sqrt{2m(E_k \cos^2(\vartheta) + V)}$, where E_k is the kinetic energy of a photoelectron and V is the inner potential. A set of ARPES spectra taken along $k_a = 0$ in the surface BZ at different photon energies ($39 \leq h\nu \leq 79 \text{ eV}$, in 2 eV steps) is converted into a (k_c, k_b, E) data set by using the inner potential $V = 13 \text{ eV}$. The $E = 0$ slice, representing the FS, is shown in Fig. 3e, and the dispersion of the states at $k_a = 0$, $k_c = -0.055 \text{ \AA}^{-1}$ is shown in Fig. 3f. We note that in this photon energy range, the 9th to the 11th BZs are probed. States localized to the surface (surface states) do not disperse with k_z and would form straight vertical streaks in Fig. 3e, if they existed.

By evaluating the volume of the FS from our ARPES measurements, V_{FS} , we can estimate the carrier concentration in our samples, $n = 2 \cdot V_{\text{FS}} / (2\pi)^3$, in the low 10^{18} cm^{-3} range. Here, we have taken into account the spin degeneracy.